Commun. Theor. Phys. **77** (2025) 045401 (7pp) https://doi.org/10.1088/1572-9494/ad8db9

The gravitational redshift effect of quantum matter waves passing a binary black hole

Qiyun Fu and Tieyan Si*

School of Physics, Harbin Institute of Technology, Harbin 150080, China

E-mail: tieyansi@hit.edu.cn

Received 1 September 2024, revised 27 October 2024
Accepted for publication 31 October 2024
Published 20 December 2024

Abstract

We simulate the gravitational redshift of quantum matter waves with a long de Broglie wavelength by tracing particle beams along geodesics, when they propagate within the rotation plane of binary black holes. The angular momentum of the binary black hole causes an asymmetric gravitational redshift distribution around the two black holes. The gravitational redshift changes the frequency of quantum matter waves and their wavelength, resulting in the different interference patterns of quantum matter waves with respect to different wavelengths. The interference pattern demonstrates strong contrast intensity and spatial order with respect to different wavelengths and the rotational angle of the binary black hole. A bright semicircular arc emerges from the interference pattern to bridge the two black holes, when they rotate to certain angles, which provides a theoretical understanding on the gravitational lensing effect of quantum matter waves.

Keywords: gravitational lensing, the binary black hole, wave inteference

1. Introduction

A moving quantum particle travels along a curved geodesic path in the vicinity of a massive celestial body, due to the highly curved spacetime. The strong gravitational field acts as a gravitational lens, focusing many photons along curved geodesic paths onto one point. The shape of light source is usually highly distorted by a gravitational lens, sometimes projecting multiple images of the same light sources [1, 2]. A ring of light sources, named the Einstein ring, is observed, when the observer, the gravitational lens and the light source are aligned in a straight line [3–5]. In most cases, the observer, gravitational lens and light source are not in a straight line, then the image of the light source is divided into multiple copies [6, 7], and is highly amplified by the convergence of light [8]. When the wavelength of the electromagnetic wave is comparable to the Schwarzschild radius of the gravitational lens, the distant light source is not distinguishable by the telescope, the Einstein ring is no longer observable [9–11]. In that case, the interference, diffraction or reflection effect of long waves becomes the apparent physical effect.

Besides electromagnetic waves with long wavelength, the gravitational wave produced by merging two black holes (or two massive neutron stars) also has a long wavelength, which is comparable to the distance between the binary stars, leading to the apparent gravitational lensing effect [12–17]. In the gravitational lensing effect of binary stars, one of the binary stars acts as a radiation source for electromagnetic waves, while the other star acts as a gravitational lens that converges electromagnetic waves [18–20]. The wave optical effects of gravitational lensing provides a basic method for the study of exoplanets [21].

The orbital velocity of the binary black holes around their mass center is large enough to distort the light path away from classical optical path [22]. We apply the numerical method of ray tracing, which was used for simulating the electromagnetic field distribution around binary black holes [23], to find the convergence path of waves in the vicinity of a binary black hole. Similar to the gravitational redshift caused by a single black hole, electromagnetic waves emitted by the surrounding objects around the binary black hole also has a gravitational shift in the perpendicular direction to the rotating plane [24–27].

We simulate the gravitational redshift of the quantum matter wave within the rotating plane of the binary black hole instead of the normal direction of the rotating plane, based on the analytic solution of the binary black hole [28, 29]. The directed rotation of the binary black hole breaks the spherical

* Author to whom any correspondence should be addressed.

symmetry of a single black hole and results in asymmetric trajectories of waves around the binary black hole, leading to the asymmetric gravitation redshift effect. The propagation paths of quantum particles in binary black hole spacetime are traced numerically by the geodesic equation. Parallel waves out of the same source interferant with one another, when they intersect at the same point. Unlike the constant frequency of waves in Euclidean spacetime, the frequency of the wave in the spacetime of the binary black hole is no longer a constant, the gravitational redshift has a strong influence on the interference patterns of intersecting waves. This article is organized into two sections: in section 2, we study the asymmetric distribution of gravitational redshift around the binary black hole and in section 3, the diffraction and interference of quantum matter waves in vicinity of the binary black hole is computed.

2. The gravitational redshift around binary black hole

The frequency of a quantum matter wave traveling from a stationary point 'o' to a moving point 'p' in curved spacetime is

$$\omega = -K^a U^b g_{ab}, \tag{1}$$

where K^a is the wave vector, U^b is the 4-dimensional velocity of the observer, and g_{ab} is the metric of the point. The frequencies measured by the moving observers are denoted as, $\omega_{\rm o}$ and $\omega_{\rm p}$. The wave vector along the world line of point 'o' is $K^a|_{\rm o} = (\omega, \vec{k})$, where $k^2 = \omega^2$. The velocity of the moving observer is $U^a|_{\rm o} = (\gamma, \gamma\vec{u})$, where $\gamma = 1/\sqrt{1-u^2}$. The quantum matter wave propagates in the positive direction of the x-axis. In the stationary coordinate system (t, r, θ, φ) of the Schwarzschild black hole

$$\begin{aligned} {\rm d}s^2 = &-(1-2M/r){\rm d}t^2 + (1-2M/r)^{-1}{\rm d}r^2 \\ &+ r^2({\rm d}\theta^2 + \sin^2\theta {\rm d}\varphi^2). \end{aligned} \tag{2}$$

The wave vector of point 'o' at infinity is $K^a|_{\rm o} = \omega(1, -1, 0, 0)$. The frequency measured by the moving observer at point 'o' is

$$\omega_{\rm o} = \gamma\omega(1-u). \tag{3}$$

The wave vector in Schwarzschild spacetime reads

$$K^a|_{\rm p} = \left(\frac{\omega}{1-\frac{2M}{r}}, -\omega, 0, 0\right), \tag{4}$$

where the distance between point 'p' and the black hole is r. Substituting the 4-dimensional velocity equation

$$U^a|_{\rm p} = \frac{1}{\sqrt{1-\frac{u^2}{\left(1-\frac{2M}{r}\right)^2}}}\frac{1}{\sqrt{1-\frac{2M}{r}}}(1, -u, 0, 0) \tag{5}$$

into frequency (1) yields the frequency of quantum matter wave at point 'p',

$$\omega_{\rm p} = \frac{\omega}{\sqrt{1-\frac{2M}{r'}}}\sqrt{\frac{1-\frac{2M}{r'}-u}{1-\frac{2M}{r'}+u}}. \tag{6}$$

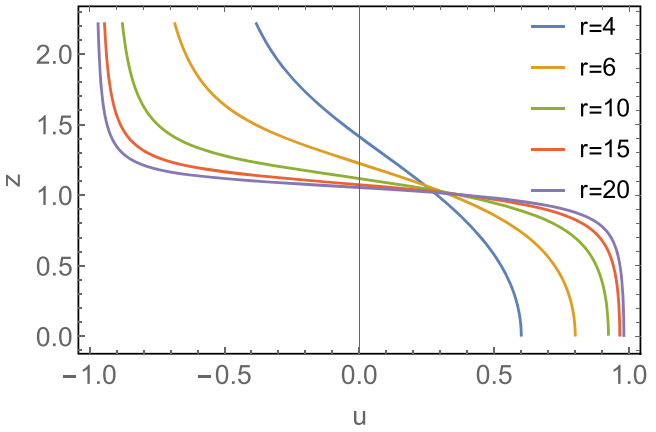

Figure 1. A Schwarzschild black hole at r from the stationary observer, moves toward the observer at a velocity of u. The redshift $z = \omega_p/\omega_o$ measured by the observer is related to distance r and relative velocity u.

The gravitational redshift is the ratio of frequency at point 'p' to the frequency (3) at point 'o',

$$\frac{\omega_{\rm p}}{\omega_{\rm o}} = \frac{1}{\sqrt{1-\frac{2M}{r}\sqrt{1-u^2}}}\sqrt{\frac{1-\frac{2M}{r}\sqrt{1-u^2}-u}{1-\frac{2M}{r}\sqrt{1-u^2}+u}}. \tag{7}$$

Equation (7) describes the gravitational redshift of quantum matter wave propagating in the positive direction x-axis with frequency $\omega_{\rm o}$. In the meantime, the Schwarzschild black hole moves toward the negative direction of the x-axis at a velocity of u. Figure 1 shows the redshift, defined by $z = \omega_{\rm p}/\omega_{\rm o}$, with respect to different distances r and incoming velocity u. The quantum matter wave experienced gravitational redshift when a black hole approaches the observer, and a gravitational blueshift when it moves away from the observer. Notice here this gravitational redshift (blueshift) is not the conventional Doppler effect.

The gravitational redshift equation above holds for a single black hole. The redshift factor on apparent horizons of a binary black hole was numerical simulated for quasicircular binary inspirals [30]. Here we calculated the gravitational redshift based on an approximated solution of the binary black hole [28]. For two black holes circling around their common center of mass, the curved spacetime around a binary black hole is described by an approximated solution [28]. The frequencies $\omega = -K^\mu Z^\nu g_{\mu\nu}$ of the matter wave at a spacetime point in the centroid system is derived from the geodesic equation, where $Z^a = (1/\sqrt{-g_{00}}, 0, 0, 0)$ is the velocity of the stationary observer. The wave vector K^μ is the tangent vector of the geodesic line. The gravitation redshift is defined by the frequency ratio of $\omega_{\rm p}$ at the point 'p' in the far region to the $\omega_{\rm o}$ in vicinity of the binary black hole, $z = \omega_{\rm p}/\omega_{\rm o}$. The incoming waves are travelling along parallel geodesic lines from the negative infinity of the y-axis, propagating toward the positive direction of the y-axis, which

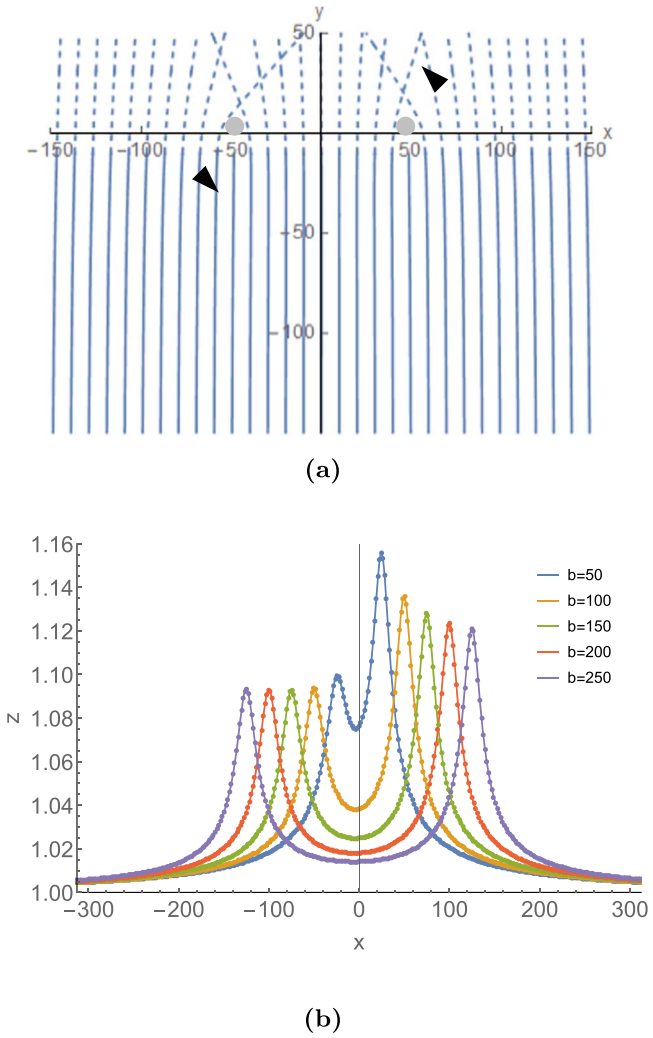

Figure 2. (a) The parallel geodesic lines from the negative infinity reaches $y=-10$. (b) The distribution of the redshift $z=\omega'_{\rm p}/\omega_{\rm o}$ on the $y=-10$ line with respect to x. b is the distance between the two black holes.

reaches the x-axis at $t=0$. The two black holes are located exactly at the x-axis in figure 2(a). The geodesic lines near the event horizon bend into different directions around the two rotating black holes, as shown in figure 2(a), where the two black holes are located at $x=\pm 50$ and rotates in the counterclockwise direction. The distribution of the gravitational redshift around the two rotating black holes at time $t=-10$ are shown in figure 2(b). The black hole at $x=-50$ moves towards the particle source, inducing a smaller blueshift than that induced by the black hole at $x=50$, which moves away from the particle source.

Figure 2(b) shows the gravitational redshift, which is numerically calculated by the geodesic equation and the approximated solution of the binary black hole [28]. The left and right maximal redshifts in figure 2(b) are 1.094 and 1.136, which are generated by two black holes separated by a distance of $b=50$. The left black hole moves towards the matter wave source at a velocity of $u=0.071$. The right black hole moves away from the matter wave source at velocity of

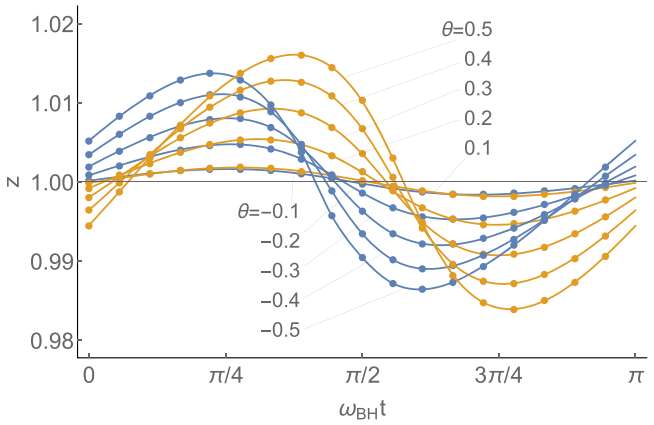

Figure 3. The evolution of redshift $z=\omega_{\rm p}/\omega_{\rm o}$ observed on Earth within half a period. $\omega_{\rm BH}$ is the angular velocity of binary black hole. The blue line represents quantum matter wave passing through the negative zone $x<0$. The red line represents quantum matter wave passing through the positive zone $x>0$. Different curves represents quantum particle beam rays with different deflection angles.

$u=-0.071$. Two approximated gravitational redshifts are derived by substituting the velocities of the two black holes into the frequency ratio equation (7), $z=1.098$ and $z=1.138$, which is consistent with the numerical result. The gravitational redshift on the left and the right side are not symmetrically distributed due to the rotation of the binary black holes. When the distance between the two black holes grows from $b=50$ to $b=250$, the gravitational redshift gradually decays (figure 2(b)).

The gravitational redshift oscillates periodically from redshift to blueshift (or vice versa) with respect to the rotating angle of the binary black hole (figure 3). For fixed locations of the matter wave source, the binary black hole and the Earth, each oscillating curve of redshift in figure 3 represents the redshift of a matter wave deflected by an angle of θ, i.e. the angle between the outgoing beam and the incoming beam. The blue curves represent the matter wave from the negative x zone ($x<-50$), and the red curves represent the matter wave from the positive x zone $x>50$. The redshift is zero at zero deflection angle $\theta\to 0$ in figure 3, i.e. $z\to 1$. The redshift grows with respect to a growing deflection angle. The maximum redshift is of 1% at $\theta=0.4$.

3. The diffraction and interference of quantum matter waves in vicinity of the binary black hole

We consider two Schwarzschild black holes that are far apart but orbiting around each other. The wave propagation, that is confined in the orbital plane of the binary black holes, is simulated based on an approximated metric solution of binary black hole [28]. The center of mass of the binary black hole is located at the origin of the coordinates. The projected metric $g_{\mu\nu}$ of the binary black hole metric to the orbital plane is

expressed by Cartesian coordinate (t, x, y),

$$\begin{aligned} g_{00} &= -1 + \frac{2m_1}{r_1} + \frac{2m_2}{r_2} - 2\left(\frac{m_1}{r_1} + \frac{m_2}{r_2}\right)^2 \\ &\quad + \frac{m_1}{r_1}[4v_1^2 - (\boldsymbol{n}_1 \cdot \boldsymbol{v}_1)^2] + \frac{m_2}{r_2}[4v_2^2 - (\boldsymbol{n}_2 \cdot \boldsymbol{v}_2)^2] \\ &\quad - 2\frac{m_1 m_2}{b}\left(\frac{1}{r_1} + \frac{1}{r_2}\right) + \frac{m_1 m_2}{b^3}\boldsymbol{b} \cdot (\boldsymbol{n}_1 - \boldsymbol{n}_2), \\ g_{0i} &= -4\left(\frac{m_1}{r_1}v_1^i + \frac{m_2}{r_2}v_2^i\right), \\ g_{ij} &= \delta_{ij}\left(1 + \frac{2m_1}{r_1} + \frac{2m_2}{r_2}\right). \end{aligned} \tag{8}$$

The two black holes at $t = 0$ are initially located at $\boldsymbol{x}_1 = (-b/2,\ 0,\ 0)$ and $\boldsymbol{x}_2 = (b/2,\ 0,\ 0)$. r_q is the distance between a location point and the qth black hole,

$$\begin{aligned} r_q &= |\boldsymbol{x} - \boldsymbol{x}_q|, \quad \boldsymbol{n}_q = \frac{\boldsymbol{x} - \boldsymbol{x}_q}{r_q}, \\ \boldsymbol{v}_q &= \frac{\mathrm{d}\boldsymbol{x}_q}{\mathrm{d}t}, \quad v_q = |\boldsymbol{v}_q|, \quad q = 1, 2. \end{aligned} \tag{9}$$

$\boldsymbol{v}_q$ is the velocity of the qth black hole. The geodesic path of the photon in the vicinity of the black hole is derived from the geodesic equation,

$$\begin{aligned} &\frac{\mathrm{d}^2 x^\mu}{\mathrm{d}s^2} + \Gamma^\mu_{\nu\sigma}\frac{\mathrm{d}x^\nu}{\mathrm{d}s}\frac{\mathrm{d}x^\sigma}{\mathrm{d}s} = 0, \\ &\Gamma^\alpha_{\lambda\mu} = \frac{1}{2}g^{\alpha\nu}(g_{\mu\nu,\lambda} + g_{\nu\lambda,\mu} - g_{\lambda\mu,\nu}). \end{aligned} \tag{10}$$

The geodesic equation is reexpressed as a first-order ordinary differential equation by introducing $u^\mu = \mathrm{d}x^\mu/\mathrm{d}s$,

$$\begin{aligned} &\frac{\mathrm{d}x}{\mathrm{d}t} = \frac{u_x}{u_t}, \quad \frac{\mathrm{d}y}{\mathrm{d}t} = \frac{u_y}{u_t}, \quad \frac{\mathrm{d}u_t}{\mathrm{d}t} = -\frac{1}{u_t}\Gamma^0_{\nu\sigma}u^\nu u^\sigma, \\ &\frac{\mathrm{d}u_x}{\mathrm{d}t} = -\frac{1}{u_t}\Gamma^1_{\nu\sigma}u^\nu u^\sigma, \quad \frac{\mathrm{d}u_y}{\mathrm{d}t} = -\frac{1}{u_t}\Gamma^2_{\nu\sigma}u^\nu u^\sigma. \end{aligned} \tag{11}$$

The geodesic path is derived from the numerical solution of $[x(t),\ y(t)]$ in equation (11).

The incoming quantum waves bend their paths in the vicinity of the binary black hole (figure 4), showing similar but different diffraction phenomena from that of electromagnetic waves. We choose the following initial parameters: the initial mass of the two black holes $m_1 = m_2 = 1$, the distance between the two black holes $b = 100$, the orbital period $T_{\mathrm{BH}} = 4443$ and the angular velocity $\omega_{\mathrm{BH}} = \sqrt{2}/1000$. The incoming monochromatic quantum matter wave is assumed to come from infinity. The two black holes are far separated from each other. The fully absorbed waves by the two black holes occupy a negligible small portion of the incoming wave. Figure 4 shows the paths of waves, when the relative position vector of the binary black hole $\boldsymbol{r}_{12} = \boldsymbol{x}_1 - \boldsymbol{x}_2$ rotates to an angle of $\pi/2$ (in figure 4(a)), $\pi/4$ (in figure 4(b)) and $\pm\pi$ (in figure 4(c)) from the incoming wave vector $\boldsymbol{k}$. The unabsorbed incoming waves on the left (right) handed side bend to the right (left) hand side when they propagate in the perpendicular direction of $\boldsymbol{r}_{12}$ in figure 4(a). The incoming

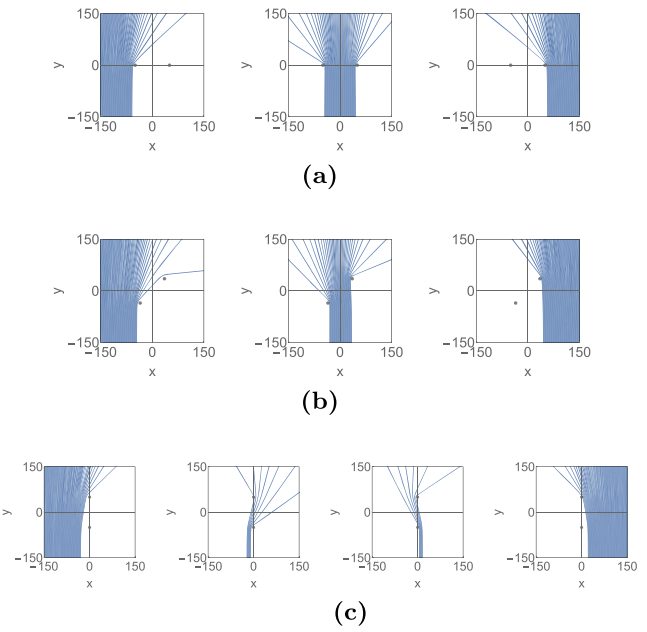

Figure 4. The diffraction paths of incoming parallel waves from infinity bend according to the angle between the relative position vector of the two black holes and the incoming wave vector, (a) $\pi/2$, (b) $\pi/4$, and (c) $\pm\pi$.

wave passing through the middle zone between two black holes spreads into a symmetric fan shaped output beams in figure 4(a). When the binary black hole rotates by an angle of $\pi/4$, the diffraction of long wave on the left (right) handed side of the black hole No. 1 (No. 2) is highly enhanced (suppressed). The output beams out of the middle zone demonstrates a highly asymmetric diffraction pattern in figure 4(b). When the relative position vector of the two black holes $\boldsymbol{r}_{12}$ rotates to the parallel direction to the incoming wave vector $\boldsymbol{k}$, beside the suppressed diffraction on both the left-hand and right-hand side of the two black holes, the incoming waves passing through the middle zone of the two black holes propagates forwardly in an 'S'-shaped trajectory in figure 4(c).

When the incoming quantum waves pass the left-handed, the right-handed and the middle zone of the two black holes simultaneously, they intersect with one another, resulting in interference pattern in the outgoing zone (as shown in figure 5). The outgoing wave is the superposition of three monochromatic waves within the left-handed zone, the middle zone and the right-handed zone correspondingly, in analogy with slits of the blocking board of double slits experiments,

$$S = |\sqrt{S_l}\,\mathrm{e}^{\mathrm{i}\omega t_l} + \sqrt{S_m}\,\mathrm{e}^{\mathrm{i}\omega t_m} + \sqrt{S_r}\,\mathrm{e}^{\mathrm{i}\omega t_r}|^2. \tag{12}$$

The projection screen is placed at infinity (here we choose $y = 1000$). The i-th geodesic path intersects the projection screen at $(t_i,\ x_i)$. The wave intensity is defined as the density of the geodesic: $S_i = 1/[(x_{i+1} - x_{i-1})\cos\theta_i]$, where θ_i is the angle between the geodesic path and the y-axis at the intersection point. The local time t_α, $(\alpha = l,\ m,\ r)$ is determined by the spacetime of the binary black hole. The wavelength of the incoming wave is chosen as comparable with the

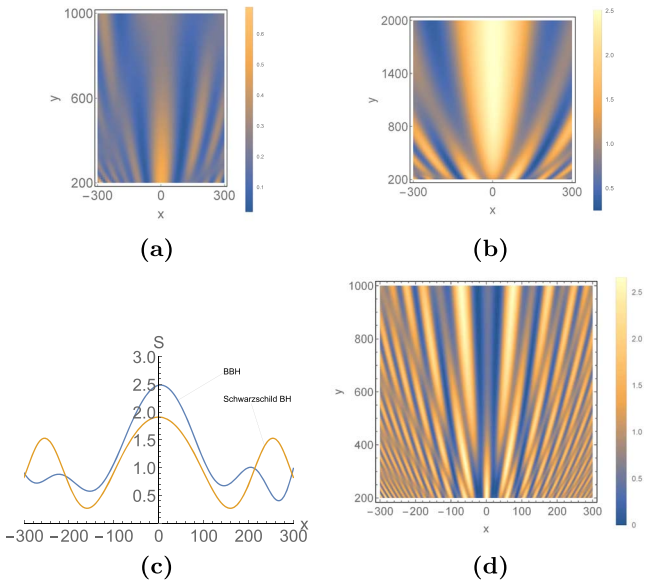

Figure 5. (a) Interference of $\lambda = 40$ monochromatic quantum wave passing through a Schwarzschild black hole with $m = 2$, (b) Interference of $\lambda = 40$ monochromatic quantum matter wave passing through a binary black hole, (c) Comparison of quantum matter wave intensity between the binary black hole and the Schwarzschild black hole, at $y = 1000$, (d) the interference of the monochromatic quantum wave with $\lambda = 10$ passing through the binary black hole.

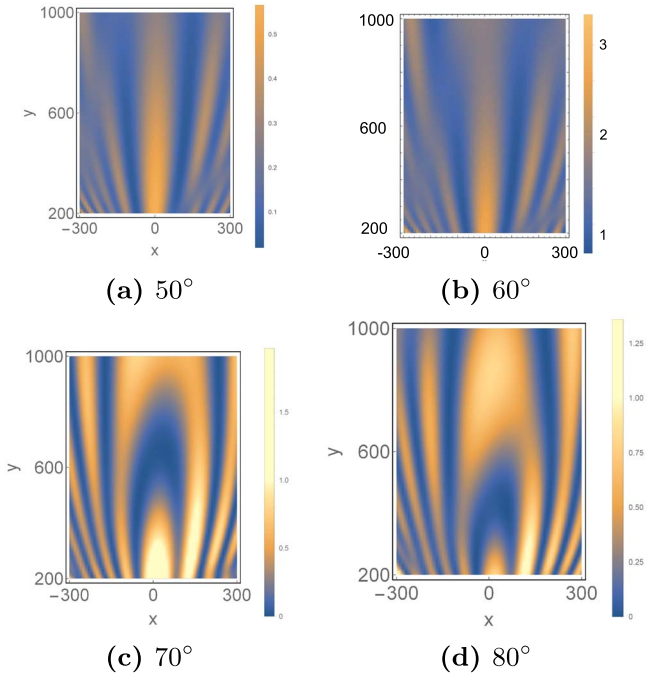

Figure 6. The interference patterns when the black hole rotates to angle of (a) 50°, (b) 60°, (c) 70° and (d) 80°.

Schwarzschild radius of a black hole in order to detect an apparat interference pattern. For a small black hole with a radius of $\lambda = 3 \times 10^3 m$, the frequency of quantum wave is $\omega = 10^5$ Hz. The spatial distribution of the amplitude of interference waves in the x–y plane is numerically computed by moving the location of the projection screen continuously, as shown in figure 5, the bright (dark) region has higher (lower) intensity. This interference pattern on a light-like hypersurface is derived from the same set of geodesics. Figure 5(a) shows the interference patterns of long waves with $\lambda = 40$ (dimensionless) passing through one Schwarzschild black hole with $m = 2$ at $x = 0$. The brightest wave packet propagates along the y-axis at $x = 0$, accompanied by two second brightest peaks in the left-hand and the right-hand regions. When the same set of long waves pass through a binary black hole (figure 5(b)), the brightest wave packet is widened but still travels along the perpendicular line to the bonding vector that connects the two black holes $\boldsymbol{r}_{12}$. The central peak is generated by the superposition of waves with the same phase, since the incoming waves from both the left-hand-side and right-hand-side travel over the same distance to reach the perpendicular line. The dimensionless relative wave intensity approaches to 2 at infinity. The second brightest peaks are highly suppressed, as shown in figure 5(b). The convergence effect of the binary black hole is stronger than single black hole. Figure 5(c) showed the spatial distribution of intensity, the central peak in the outgoing zone of the binary black hole decays faster than that of a single black hole.

The maximal peak of the superposition waves after passing single black hole is always along the middle line despite of wavelengths, i.e. the y-axis at $x = 0$ (figure 5(a)). However the interference pattern in the outgoing zone of binary black hole has strong dependence on the wavelength of the incoming waves. Figure 5(d) showed the interference pattern of incoming waves with a relatively short wavelength $\lambda = 10$. In the near zone of the binary black hole, the maximal peak is still located along the middle line. The brightest peak decays as the observer travels away from the binary black hole, so does the other bright peaks. On the contrary, the intensity of the dark peaks grow to become the bright peaks in the far zone of the binary black hole. Therefore the intensity of superposition waves along the perpendicular line to the bonding line between the two black holes is only strengthened in the near zone, and is reduced to zero in the far zone of the binary black hole.

The two black holes are located along x-axis in figure 5, i.e. the angle between the relative position vector $\boldsymbol{r}_{12}$ and x-axis is 0°. The interference pattern shows different spatial distribution when the bonding vector $\boldsymbol{r}_{12}$ rotates to 50°, 60°, 70° and 80°, as showed in figure 6. When the bonding vector is further tilled to 50° and 60°, the outgoing waves split into straight rays distributed in bright and dark pattern alternatively. These straight rays decays in a straight way to infinity (figures 6(a)–(b)). When the bonding vector is further tilled to 70°, the bright rays generates by interference bend into parabolic arcs that bridges the two black holes (figure 6(c)). A further rotation of $\boldsymbol{r}_{12}$ to 80° draws the bright ray bridge closer to the binary black hole. In the meantime, the intensity of the outgoing wave becomes more than ten times stronger (figure 6(d)).

The intensity of interference pattern changes with respect to different wavelengths and phase differences of the incoming waves. For single black hole, the intensity of

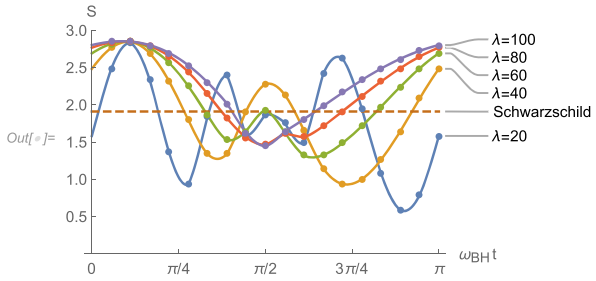

Figure 7. The evolution of interference intensity at different wavelengths over time at point (0, 1000).

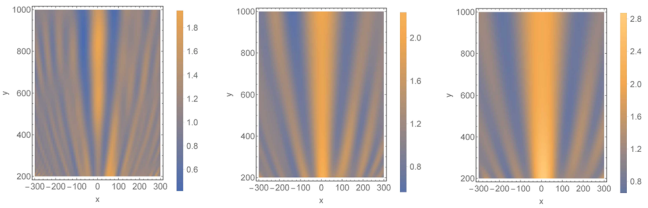

Figure 8. The average interference intensity of quantum matter wave in one orbital period. (a) $\lambda = 20$ (b) $\lambda = 40$ (c) $\lambda = 60$.

interference pattern is independent of wavelength (as shown by the dash line in figure 7). At a point $(x, y) = (0, 1000)$ in the outgoing zone, the light intensity oscillates with different wavelengths, as shown in figure 7. A minimal intensity locates at the $\theta = \omega_H t = \pi/2$ in figure 7. The number of periodical oscillations increases when the wavelength is reduced (figure 7).

We average the quantum wave intensity, which is a function of spacetime coordinates $S(t, x, y)$, at every point within a binary black hole orbit period,

$$\overline{S}(x, y) = \frac{1}{n}\sum_{i=1}^{n} S(t_i, x, y). \tag{13}$$

The average wave intensity always shows a maximum value along the y-axis. The central bright fringe sandwiched in between two dark fringes is most obvious for the short wavelength (figure 8). The width of the central bright fringe widens when the wavelength increases, from $\lambda = 20$, to $\lambda = 40$ and $\lambda = 60$ (figures 8(a), (b), (c)). The width of the central bright fringe generated by the lens effect of two black holes is wider than that of a single Schwarzschild black hole, which approximately obeys $\Delta x \propto \sqrt{y}$. The width of the central bright fringe of the binary black hole increases slowly, when the observer moves away from the binary black hole, as shown in figure 8. On the detection screen at $y = 1000$, the width of the central bright fringe of the average wave intensity in figure 9 is approximately fitted by $\Delta x \propto a\sqrt{\lambda} + b$, with fitting parameter $a = 67.8$, $b = -110$ for a single Schwarzschild black hole and $a = 65.8$, $b = -134$ for the binary black holes (figure 9). The intensity of the central bright fringe increases with the increasing of incoming wavelength. The peak intensities are $\overline{S}_{\max} =$ 1.75, 1.82, 2.20, 2.43, 2.62 with respect to $\lambda = 20$, 40, 60, 80, 100.

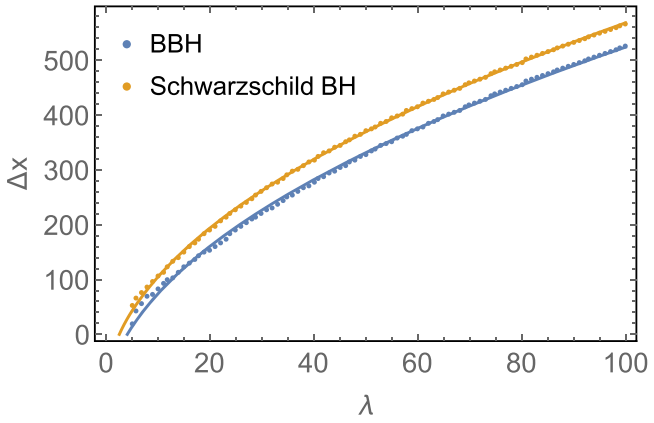

Figure 9. The width of the central bright fringe as a function of the wavelength of the incident quantum matter wave.

4. Conclusions

When the two black holes rotate around their common center of mass, the two black holes result in opposite gravitation redshift, i.e. the gravitational redshift (blueshift) due to the left (right) black hole. The angular velocity of the binary black hole determines the asymmetric distribution of gravitational redshift. The amplitude of redshift is positively correlated to the deflection angle of the incoming matter wave. Propagating waves inference one another when curved geodesics of a binary black hole intersect with one another. The interference fringes of binary black holes have a bright central stripe accompanied by two dark adjacent stripes. Unlike the interference pattern of electromagnetic waves passing thorough double slits, the relative intensity of the bright and dark strips in the interference pattern of the quantum matter wave passing through a binary black hole does not decease to zero, instead it preserves to infinity, providing a promising observation on Earth. As the binary black hole rotates, the bright central stripe turn into dark strip, while the adjacent dark stripes remain dark all the time. The average interference fringe is obtained by overlaying the interference fringes within an orbital period. Compared with a single black hole, the bright central stripe concentrates more energy, and the peak intensity of the central bright stripe is always larger than that of a single black hole.

References

[1] Inada N *et al* 2003 A gravitationally lensed quasar with quadruple images separated by 14.62 arcseconds *Nature* **426** 810–2
[2] Inada N *et al* 2006 SDSS J1029 + 2623: a gravitationally lensed quasar with an image separation of 22.5 *Astrophys. J. Lett.* **653** L97
[3] Bartel N 1978 Direct observation of pulsar microstructure at timescales down to 6 microseconds *Astron. Astrophys.* **62** 393
[4] Lange C, Kramer M, Wielebinski R and Jessner A 1998 Radio pulsar microstructure at 1.41 and 4.85 GHz *Astron. Astrophys.* **332** 111
[5] Lyutikov M 2004 On the nature of eclipses in binary pulsar J0737-3039 *Mon. Not. R. Astron. Soc.* **353** 1095

[6] Jana S, Kapadia S J and Venumadhav T 2023 Cosmography using strongly lensed gravitational waves from binary black holes *Phys. Rev. Lett.* **130** 26
[7] Sonnenfeld A 2021 Statistical strong lensing-II. Cosmology and galaxy structure with time-delay lenses *Astron. Astrophys.* **656** A153
[8] Refsdal S and Bondi H 1964 The gravitational lens effect *Mon. Not. R. Astron. Soc.* **128** 295–306
[9] Ohanian H C 1974 On the focusing of gravitational radiation *Int. J. Theor. Phys.* **9** 425
[10] Ohanian H C 1983 The caustics of gravitational lenses *Astrophys. J.* **271** 551
[11] Deguchi S and Watson W D 1986 Wave effects in gravitational lensing of electromagnetic radiation *Phys. Rev.* D **34** 1708
[12] Naderi T, Mehrabi A and Rahvar S 2018 Primordial black hole detection through diffractive microlensing *Phys. Rev.* D **97** 103507
[13] Oguri M and Takahashi R 2022 Amplitude and phase fluctuations of gravitational waves magnified by strong gravitational lensing *Phys. Rev.* D **106** 043532
[14] Cusin G and Lagos M 2020 Gravitational wave propagation beyond geometric optics *Phys. Rev.* D **101** 044041
[15] Wei S W and Liu Y X 2014 Establishing a universal relation between gravitational waves and black hole lensing *Phys. Rev.* D **89** 047502
[16] Hou S, Fan X and Liao K 2020 Gravitational wave interference via gravitational lensing: measurements of luminosity distance, lens mass, and cosmological parameters *Phys. Rev.* D **101** 064011
[17] Suyama T, Takahashi R and Michikoshi S 2005 Wave propagation in a weak gravitational field and the validity of the thin lens approximation *Phys. Rev.* D **72** 043001
[18] Pen U L and Yang I S 2015 Strong lensing interferometry for compact binaries *Phys. Rev.* D **91** 064044
[19] Mao S 1992 Gravitational lensing, time delay, and gamma-ray bursts *Astrophys. J. Lett.* **389** L41
[20] Smits R, Kramer M and Stappers B 2009 Pulsar searches and timing with the square kilometre array *Astron. Astrophys.* **493** 1161
[21] Mehrabi A and Rahvar S 2013 Studying wave optics in exoplanet microlensing light curves *Mon. Not. R. Astron. Soc.* **431** 1264
[22] Frittelli S and Newman E T 2002 Dynamics of Fermat potentials in nonperturbative gravitational lensing *Phys. Rev.* D **65** 123006
[23] Bohn A, Throwe W and Hébert F 2015 What does a binary black hole merger look like? *Class Quantum Grav.* **32** 065002
[24] Detweiler S 2008 Consequence of the gravitational self-force for circular orbits of the Schwarzschild geometry *Phys. Rev.* D **77** 124026
[25] Sago N, Barack L and Detweiler S 2008 Two approaches for the gravitational self-force in black hole spacetime: comparison of numerical results *Phys. Rev.* D **78** 124024
[26] Shah A G *et al* 2011 Conservative, gravitational self-force for a particle in circular orbit around a Schwarzschild black hole in a radiation gauge *Phys. Rev.* D **83** 064018
[27] Zimmerman A, Lewis A G M and Pfeiffer H P 2016 Redshift factor and the first law of binary black hole mechanics in numerical simulations *Phys. Rev. Lett.* **117** 191101
[28] Alvi K 2000 Approximate binary-black-hole metric *Phys. Rev.* D **61** 124013
[29] Astorino M and Vigano A 2021 Binary black hole system at equilibrium *Phys. Lett.* B **820** 136506
[30] Zimmerman A, Lewis A G M and Pfeiffer H P 2016 Redshift factor and the first law of binary black hole mechanics in numerical simulations *Phys. Rev. Lett.* **117** 191101